ADVANCED FUNCTIONAL MATERIALS
www.afm-journal.de

Cs-Doped and Cs-S Co-Doped CuI p-Type Transparent Semiconductors with Enhanced Conductivity

Adeem S. Mirza, Badri Vishal, Pia Dally, Claudia S. Schnohr, Stefaan De Wolf, and Monica Morales-Masis**

One hindrance in transparent electronics is the lack of high-performance p-type transparent conductors (TCs). The state-of-the-art p-type TC, CuI, has a conductivity two orders of magnitude lower than n-type TCs like ITO. While doping strategies have shown promise in enhancing the hole carrier density in CuI, they often come at the expense of hole mobility. Therefore, understanding how extrinsic dopants affect the mobility of CuI is critical to further improve the performance of CuI-based TCs. Here the structural and electronic properties of Cs-doped CuI are investigated. It is demonstrated that ≈4 at.% Cs doping in CuI increases the carrier density from 2.1 × 10^{19} to 3.8 × 10^{20} cm^{-3} while preserving the film microstructure and local coordination of Cu, as confirmed by HRTEM and XAS analysis. Introducing S as a co-dopant in Cs:CuI boosts the carrier density to 8.2 × 10^{20} cm^{-3}, reaching a stable conductivity of ≈450 S cm^{-1}. In all cases, the enhanced carrier density negatively affects the hole mobility with ionized impurity scattering and increased Seebeck hole effective mass as mobility limiting mechanisms. Nonetheless, the new Cs, S co-doped CuI exhibits high p-type conductivity, Vis–NIR transparency, and stability, presenting an attractive candidate for future transparent electronic devices.

1. Introduction

The advent of transparent conductors (TCs) has brought upon us an emerging field of transparent electronics, which include displays, semi-transparent solar cells, and smart windows. Currently, we rely on n-type TCs which are mostly degenerately doped post-transition metal oxides, with tin-doped indium oxide (ITO) being the archetypical n-type TC presenting a bandgap > 3 eV and conductivities (σ_h) reaching 10^4 S cm^{-1}.[1,2] Contrarily, wide band gap (E_g) p-type TCs are still limited to σ_h values in the order of 10^2 S cm^{-1} or below, which is a major hurdle in achieving fully transparent electronics.[3,4] Among p-type TCs, doped copper iodide (CuI) is among the highest-performing TCs in terms of conductivity. Recently, interest in CuI has resurged owing to its wide E_g and possible extrinsic and intrinsic p-type doping. Moreover, reported high Seebeck coefficient (α) > 200 μV K^{-1} makes it interesting for, for example, transparent thermoelectrics.[5–8]

Intrinsic CuI typically exhibits a σ_h ≈50 S cm^{-1},[9] with reported experimental hole mobility (μ_h) values ranging from ≈20 to ≈44 cm^2 V^{-1} s^{-1} for single crystals,[10,11] and ≈10 to 25 cm^2 V^{-1} s^{-1} (depending on the free hole carrier density, n_h) for polycrystalline films.[12–14] Epitaxial CuI either on Al_2O_3[15] or InAs,[16–18] yielded μ_h = 20 cm^2 V^{-1} s^{-1}, or μ_h ≈10 cm^2 V^{-1} s^{-1} as well. Regardless of the single or polycrystalline nature of CuI, the highest μ_h is always achieved for low n_h in the order of 10^{17} cm^{-3}. This suggests the presence of different scattering mechanisms at play for low and high n_h. Recently, Willis et al. modeled the charge transport mechanisms in CuI and concluded that at n_h ≈10^{16} cm^{-3}, a maximum μ_h = 162 cm^2 V^{-1} s^{-1} is achievable owing to limitations by phonon scattering, while, in the degenerately doped regime with n_h ≈10^{20} cm^{-3}, a maximum μ_h of 32.6 cm^2 V^{-1} s^{-1} is feasible, limited by the ionized impurity scattering.[19] This

A. S. Mirza, M. Morales-Masis
MESA+ Institute for Nanotechnology
University of Twente
AE Enschede 7500, The Netherlands
E-mail: a.s.mirza@utwente.nl; m.moralesmasis@utwente.nl

B. Vishal, P. Dally, S. De Wolf
KAUST Solar Center (KSC)
Physical Sciences and Engineering Division (PSE)
King Abdullah University of Science and Technology (KAUST)
Thuwal 23955, Kingdom of Saudi Arabia

C. S. Schnohr
Felix Bloch Institute for Solid State Physics
Leipzig University
Linnéstraße 5, 04103 Leipzig, Germany

The ORCID identification number(s) for the author(s) of this article can be found under https://doi.org/10.1002/adfm.202316144

DOI: 10.1002/adfm.202316144

implies higher μ_h values are possible through improving the quality of CuI films. For instance, it has been shown that high μ_h = 25 cm^2 V^{-1} s^{-1} is possible for high $n_h = 10^{19}$ cm^{-3}, if the film quality is improved.[14]

In addition to μ_h, to further improve σ_h of CuI, the n_h should be increased by, for example, introducing various dopants in the lattice.[8,20–23] Growing CuI in iodine-rich conditions has been shown to result in $n_h \approx 10^{20}$ cm^{-3}, however, there is no mention of the stability of n_h over time.[24] Extrinsic doping with Se was reported to increase n_h from $\approx 10^{15}$ to 8×10^{17} cm^{-3}.[21] S-doping is one of the most effective extrinsic dopants, resulting in high n_h of 5×10^{19} cm^{-3} < n_h < 9×10^{20} cm^{-3}).[5,8,22,23,25] Defect analysis of S-doped CuI indicated that S indirectly helps in promoting copper vacancies (V_{Cu}) by shifting the chemical potential to I-rich conditions.[8] Alternatively, Cs doping was reported to increase the n_h from $\approx 10^{14}$ to > 10^{19} cm^{-3}.[20] Alloying is another approach to achieve high σ_h, primarily increasing the $n_h > 10^{21}$ cm^{-3}.[26] Recently, record p-type TC σ_h values approaching those of n-type TCs were demonstrated for amorphous thin film Cu(S,I) alloys, with $n_h \approx 10^{22}$ cm^{-3} and $\mu_h \approx 3$ cm^2 V^{-1} s^{-1}.[27]

When it comes to the fabrication of CuI thin TCs, several techniques have been reported. One method consists of the iodination of Cu[28] or Cu_3N[9] films to form CuI or the iodination of $Cu_{2-x}S$[27] films to form an amorphous Cu(S,I) alloy. Solution processes such as spray coating,[29] inkjet printing,[30] and spin coating[31] are used for fabricating intrinsic as well as S[22] and Cs[20] doped CuI films. Last, physical vapor deposition processes including thermal evaporation,[14] reactive sputtering,[24] and molecular beam epitaxy[18] have been demonstrated for intrinsic CuI films too. Pulsed laser deposition (PLD) has been shown to be a promising technique for intrinsic CuI[15] as well as Se-doped[21] and S-doped CuI.[8]

Hitherto, Matsuzaki et al. demonstrated Cs-doped CuI films via spin coating a solution of CuI and CsI in acetonitrile resulting in an increase in σ_h to 15 S cm^{-1}.[20] However, besides low σ_h, the impact of Cs incorporation on CuI microstructure and its link to σ_h was not addressed. In this work, we show a room-temperature growth of Cs-doped CuI (Cs:CuI) films via PLD. We investigated the structural properties via X-ray diffraction (XRD 2θ-ω scan), scanning/transmission electron spectroscopy (S/TEM), and X-ray photoelectron spectroscopy (XPS) and probed into the local structure around Cu in the Cs doped CuI films with X-ray absorption near edge (XANES) and X-ray absorption fine structure (EXAFS). The optoelectronic properties are analyzed by measuring transmittance/reflectance in wavelength range 300–1500 nm, room temperature as well as temperature dependent (10–300 K) Hall effect measurements in Van der Pauw configuration and room temperature Seebeck coefficient measurements. We demonstrate a σ_h of ≈290 S cm^{-1} with visible transparency of ≈75% for 4 atomic percent (at. %) Cs incorporation in CuI films. Furthermore, a novel approach of co-doping CuI films with Cs and S (Cs,S:CuI) is demonstrated, boosting σ_h to ≈570 S cm^{-1}. Ultimately, we propose the mechanisms responsible for the drop in μ_h with the increase in n_h and examine the ambient stability of doped CuI films.

2. Results and Discussion

2.1. Morphology and Structural Properties of Cs:CuI TCs

CuI and Cs:CuI films with low and high Cs doping levels were prepared by PLD from either CuI targets (for pure CuI) or from CsI:CuI targets containing different molar ratios of CsI and CuI (for the Cs:CuI). Throughout the manuscript, we use the notation **LD-Cs:CuI** for low-doping Cs:CuI, and **HD-Cs:CuI** for high-doping Cs:CuI to define the films. As it will be explained below, LD-Cs:CuI refers to ≈1.8 at. % Cs in CuI and HD-Cs:CuI refers to ≈4 at. % Cs in CuI.

The PLD-grown CuI, LD-Cs:CuI, and HD-Cs:CuI TC films are polycrystalline with root mean square (RMS) roughness of ≈10 nm and show densely packed columnar growth (**Figure 1A–C**). The 2θ-ω symmetric scans (Figure 1D) confirm the room temperature zinc blende cubic phase of CuI (γ-CuI)[32] and the films are textured in (111) direction with no signs of strain after the addition of Cs. However, HD-Cs:CuI films stabilize a metastable monoclinic phase of CuI,[33] with a small peak emerging at 2θ–50^0. This was later confirmed by high-resolution TEM, indicating the local presence of a monoclinic phase.

To elucidate further the CuI and Cs:CuI structures, we probed the local structure around Cu using X-ray absorption spectroscopy (XAS). The Cu K-edge was measured for the intrinsic CuI and compared with that of an HD-Cs:CuI. The XANES is identical for both TCs and reveals no signs of oxidation of Cu (Figure 1E).[34] If we look at the Fourier transform of the extended EXAFS (Figure 1F), we see again the same features with nearly identical amplitudes for both films. This demonstrates that the local coordination of Cu in the HD-Cs:CuI film is the same as in intrinsic CuI. Fitting these spectra (Figure S1, Supporting Information) yields the average Cu-I bond length d and the bond length disorder σ^2, which arises from thermal vibrations and static disorder. The fit quality is excellent and we obtain $d = (2.607 \pm 0.001)$ Å and $\sigma^2 = (2.1 \pm 0.1) \times 10^{-3}$ Å^2 for intrinsic CuI, in good agreement with previous reports.[34,35] The average Cu-I bond length and bond length disorder obtained for the HD-Cs:CuI are identical to those of intrinsic CuI within the given uncertainty. This confirms that the average local structure surrounding Cu is the same for both TCs and that the crystalline quality on the sub-nanometer scale is not diminished by incorporation of up to ≈4 at. % Cs.

The elemental distribution of Cs dopant and its effects on the microstructure were examined via TEM. **Figure 2** shows high-angle annular dark field (HAADF-STEM) images with corresponding Cs elemental mapping of CuI films with overall averages of ≈1.8 at. % and ≈4 at. % Cs. The Cu and I distribution is found to be homogenous for both TCs as demonstrated in Figure S2A,B (Supporting Information). The LD-Cs:CuI film exhibits a uniform distribution of Cs, with a measured concentration of ≈1.8 at. % Cs (Figure 2A), while the HD-Cs:CuI film exhibits a non-uniform distribution of Cs both within and across the grains of the film, ranging from 2.2% to 4.5% (Figure 2B). Both, the LD-Cs:CuI and HD-Cs:CuI films consist of large grains, approximately as large as the film thickness (≈150 nm) (Figure 2C,D). Additionally, prominent lamellar microstructures are frequently observed within the majority of grains in the material contain-

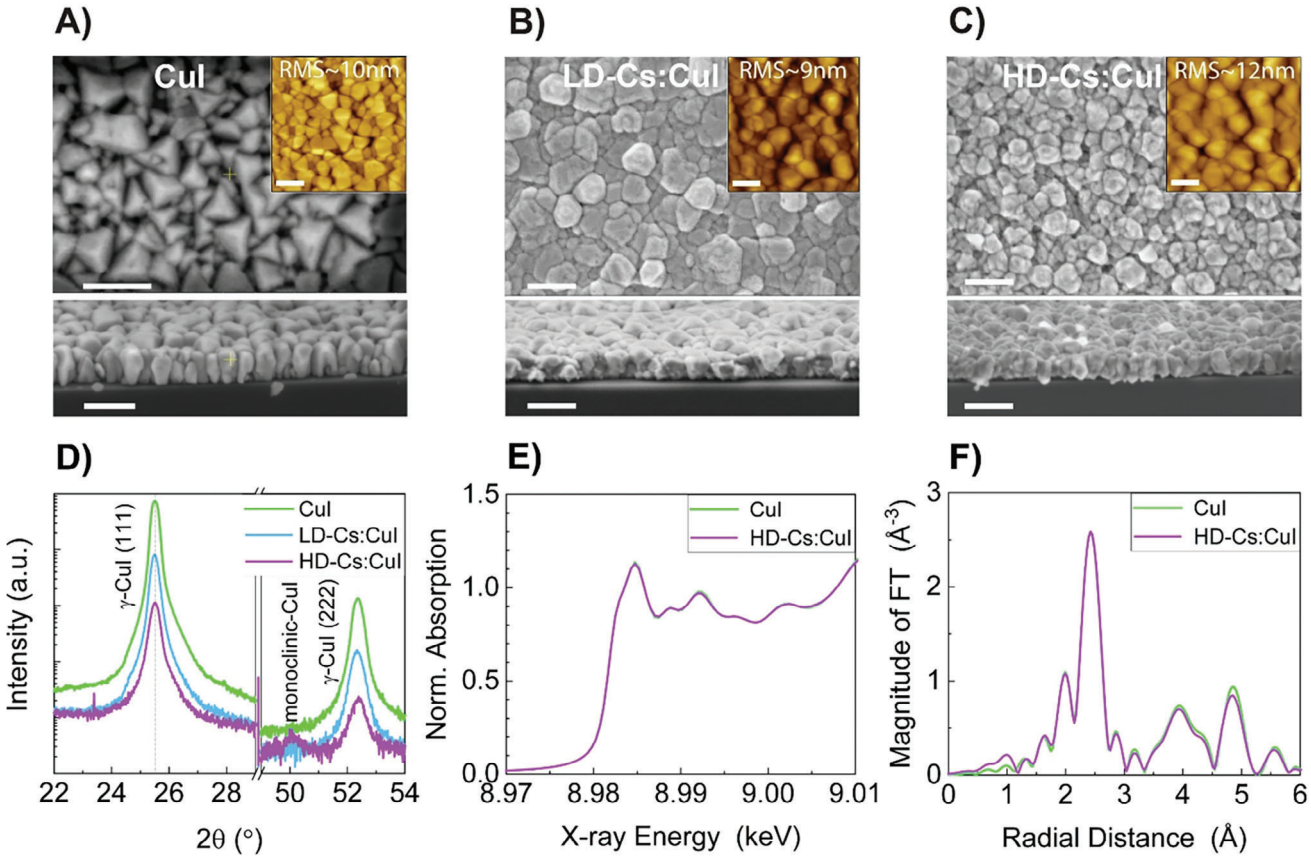

Figure 1. Morphology and structural properties of CuI and Cs:CuI TCs. SEM top view/cross-section and AFM (inset) images of A) CuI B) LD-Cs:CuI C) HD-Cs:CuI. The scale in all the figures corresponds to 200 nm. D) 2θ-ω symmetric scans of CuI based films E) XANES spectra for CuI and HD-Cs:CuI films around Cu K-edge F) Magnitude of Fourier transformed (FT) EXAFS spectra for CuI and HD-Cs:CuI films above Cu K-edge.

ing an average of 4% of Cs (indicated by arrows) (Figure 2D; Figure S2C–E, Supporting Information).

In Figure 2E, a high-magnification HRTEM image confirms the presence of a continuous grain boundary (GB) in the LD-Cs:CuI film (marked area in Figure 2C), where both grains 1 and 2 are in cubic phase (F $\bar{4}$ 3m) confirmed by taking the fast Fourier transform (FFT) image. In Figure 2F, atomically resolved HRTEM reveals the <111> plane continuing across the grain boundary, confirming endotaxial growth. The endotaxial direction of the grain aligns with the film growth direction, confirming the uniform coalescence of grains during deposition.

In Figure 2G, a high-magnification HRTEM image of the HD-Cs:CuI film reveals grain boundaries (GBs) between three cubic phases (labeled as x, y, z) confirmed by the corresponding FFT image (Figure S2D, Supporting Information). Phases x and y exhibit a nano-twinning microstructure (also see Figure S2E, Supporting Information). Twinning can result from deviations in the ideal crystal structure's lowest free energy state (here, due to lattice strain, caused by an uneven Cs distribution) and slip-along twin planes.[36] Furthermore, room temperature film growth, involving uncontrolled natural cooling from plasma to thin film, can also induce nano-twinning. In Figure 2H, a small amount of a secondary monoclinic metastable phase (P1c1) is observed locally on the top surface of HD-Cs:CuI film (marked as a square in Figure 2D), as mentioned earlier and shown in 2θ-ω scan, Figure 1D. Despite the presence of nano-structural features due to Cs dopants in the CuI lattice, it does not undergo structural transformation and predominantly remains in the parent cubic phase. Overall, from our XRD, XAS, and TEM analysis, we can conclude that the Cs-doping in small atomic percentages up to 4% does not significantly affect the crystal structure of the parent CuI lattice.

To investigate the surface chemistry, XPS was carried out on the CuI, LD-Cs:CuI, and HD-Cs:CuI films. As evident from the survey spectra (Figure S3, Supporting Information), intrinsic CuI comprises of Cu and I along with surface contaminants O and C. The estimated compositions from XPS are presented in Tables S1–S3 (Supporting Information). XPS high-resolution spectra for Cu 2p, I 3d, and Cs 3d core levels are presented in **Figure 3**. There is no significant shift in binding energies (B.E.) of Cu $2p_{3/2}$ orbitals for intrinsic CuI (932.5 eV) and both Cs:CuI TCs (932.4 eV) (Figure 3A), which is in accordance with the reported values[14,31,37–40] in the CuI system. Cu is only present in the Cu^{+} oxidation state, which is further confirmed by the absence of any satellite peak (of Cu^{2+}), a typical feature of compounds such as CuO (with Cu^{2+} species).[9] There is a shift toward lower B.E. of I $3d_{5/2}$ orbitals (Figure 3B) from 619.7 eV for CuI to 619.5 eV for both cases of Cs:CuI, suggesting the possibility of a slightly

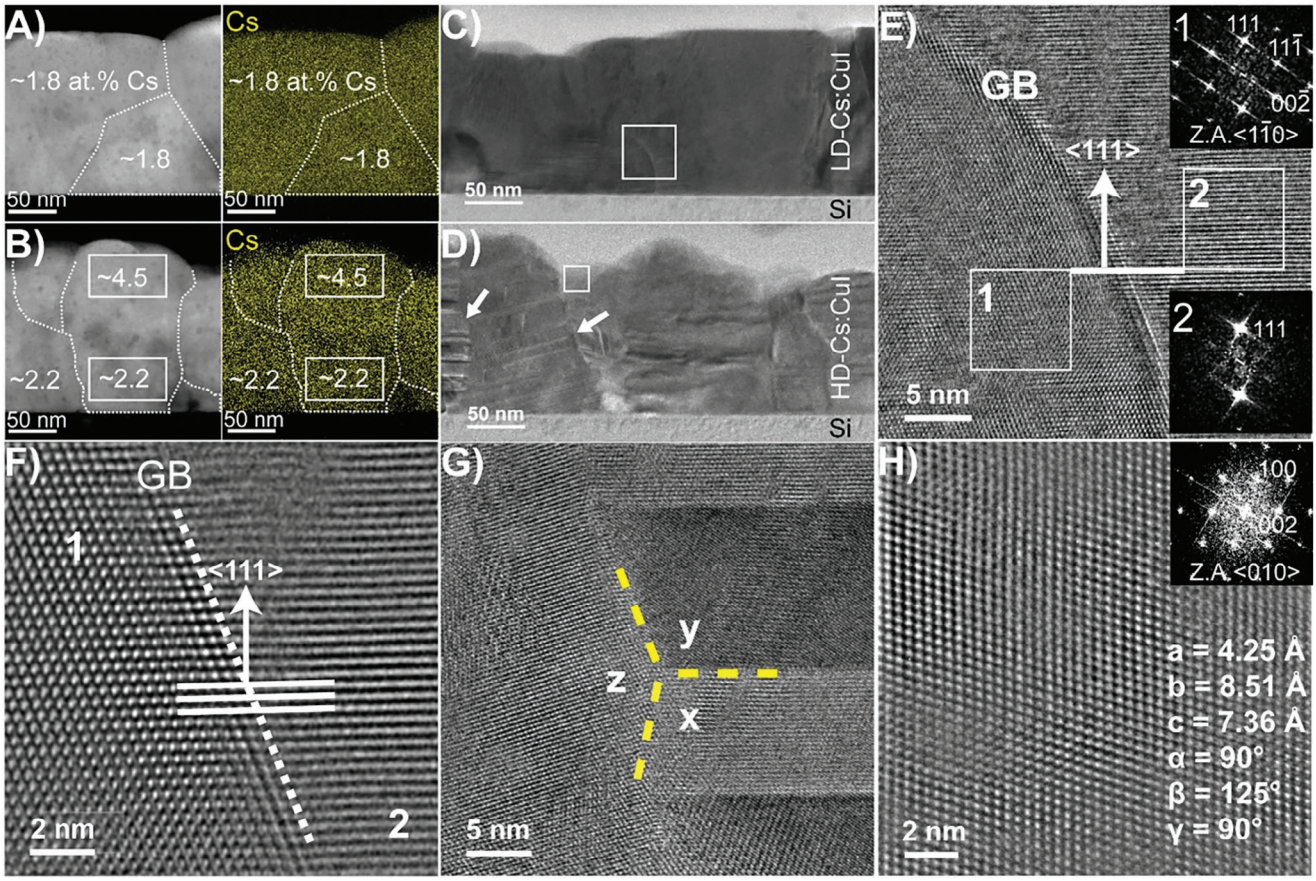

Figure 2. HAADF-STEM low and high magnification images around GBs and elemental distribution in Cs:CuI TCs A,B) HAADF-STEM and elemental mapping of LD-Cs:CuI and HD-Cs:CuI films respectively C,D) Low magnification TEM of LD-Cs:CuI and HD-Cs:CuI films respectively E) HRTEM of LD-Cs:CuI film with continuous GB between grain 1 and 2 and corresponding FFT F) Atomically resolved HRTEM of continuous atomic plane <111> at GB of LD-Cs:CuI film G) HRTEM of triple GBs between grains x, y, and z, where x and y have nano-twinning in HD-Cs:CuI film H) HRTEM and FFT of monoclinic (P1c1) metastable phase in HD-Cs:CuI film.

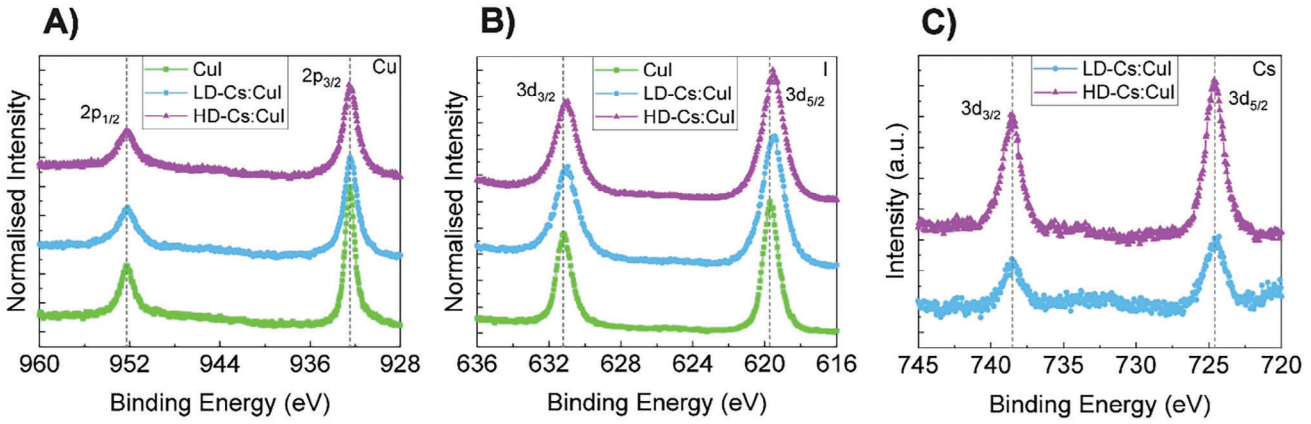

Figure 3. XPS high-resolution spectra of A) Cu 2p B) I 3d and C) Cs 3d of CuI and Cs:CuI films. For fitting parameters, refer to Table S4 (Supporting Information).

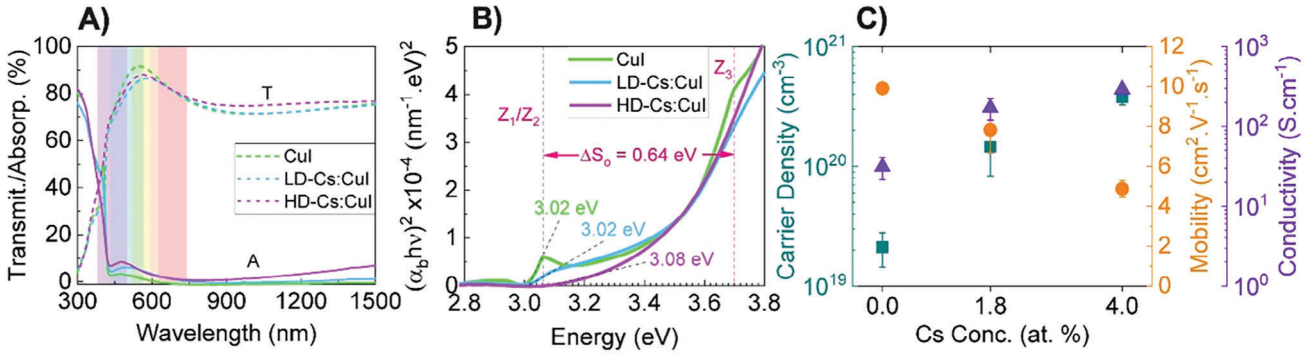

Figure 4. Optoelectronic properties of CuI and Cs:CuI TCs A) Transmittance (T) and Absorptance (A) of CuI and Cs:CuI films. A is calculated using Reflectance (R) and is defined as A = 100 − T − R. Refer to Figure S4 (Supporting Information) for R data. B) Tauc plot of the CuI and Cs:CuI TCs. For CuI, the band splitting of 0.64 eV is observed owing to spin-orbit coupling. C) Hole carrier density, hole mobility, and p-type conductivity of CuI and Cs:CuI measured via Van der Pauw configuration of Hall effect at room temperature.

I-rich surface after Cs-doping, yet the I/Cu and I/(Cs+Cu) only varies slightly as confirmed by STEM/EDX (Table S3, Supporting Information).[14,31,37] Furthermore, I stay in the I^- oxidation state.[29–31] For Cs 3d core orbitals, the B.E. of 724.6 eV for Cs $3d_{5/2}$ (Figure 3C), agrees with CsI[41–43] and as expected the absolute intensities depict higher Cs atomic percentage in the HD-Cs:CuI TC compared to the LD-Cs:CuI TC.

2.2. Optoelectronic Properties of Cs:CuI TCs

Optical properties are measured for CuI and Cs:CuI films with thicknesses ≈100 nm. The average visible transmittance (T) is unaffected by Cs-doping and remains above 75% from the Vis to the NIR range of the spectrum for all the films (**Figure** 4A). We see a slight increase in visible absorptance (A) with increasing Cs content in the Vis and NIR spectrum, but overall, it stays below 10% in the measured range (Figure 4A). The increase in near-infra-red (NIR) absorptance indicates that the Cs-doping causes an increase in the free carrier absorption (FCA), owing to an increase in the n_h, as will be discussed later. CuI is a well-known direct E_g semiconductor[8,32,44] for that the optical E_g can be estimated using the Tauc plot relation $(\alpha_b h\upsilon)^{1/\gamma}$, with Tauc exponent $\gamma = 1/2$, where α_b = absorption coefficient, h = Planck constant and υ = frequency.[45] A slight increase in E_g can be seen from 3.02 eV for CuI to 3.08 eV for HD-Cs:CuI TC, see Figure 4B. Z_1/Z_2 denotes the main band edge absorption and the characteristic peak Z_3 (only visible in the case of CuI) is associated with band splitting (due to spin-orbit interactions) of the VB.[32] Z_3 diminishes upon Cs-doping that could be ascribed to the formation of a defect band traversing in the VB (owing to large n_h)[9] or the presence of resonant states in VB[46] (owing to Cs doping). The energy difference (Z_3–Z_1/Z_2) for CuI is 0.64 eV which is consistent with the previously reported values obtained by calculations and experiments.[8,32]

Regarding the electronic properties, n_h significantly increases from 2.1×10^{19} cm^{-3} for CuI to 1.4×10^{20} cm^{-3} for LD-Cs:CuI, and even further to 3.8×10^{20} cm^{-3} for HD-Cs:CuI (Figure 4C). As reported in reference,[20] the introduction of Cs (which has the same oxidation state of Cu, i.e., +1) promotes the formation of defect complexes ($[Cs_i\text{-}3V_{Cu}\text{-}V_I]^-$ and $[Cs_i\text{-}4V_{Cu}\text{-}V_I]^{2-}$), which results in an increased density of V_{Cu} defects. V_{Cu} are energetically the most shallow defects in CuI, having the lowest formation energy among possible point defects in CuI.[8,19,32,44] The points above suggest that the density of V_{Cu} is increasing with Cs-doping. Another possibility is a decrease in compensating donor iodine vacancies (V_I) with Cs-doping, hence increasing the n_h. On the contrary, we see a decrease in the μ_h from 9.9 cm^2 V^{-1} s^{-1} for intrinsic CuI to 7.8 cm^2 V^{-1} s^{-1} for LD-Cs:CuI to 4.9 cm^2 V^{-1} s^{-1} for HD-Cs:CuI (Figure 4C). This decrease in μ_h can be attributed to increased ionized impurity scattering resulting from an increase in n_h as suggested by the temperature dependent σ measurements discussed later in Section 2.4 and Figure 7A. Overall, we achieve a σ_h of 292 S cm^{-1} for HD-Cs:CuI, which is almost a ten-fold improvement compared to 31 S cm^{-1} for intrinsic CuI.

2.3. The Case of Cesium and Sulfur Co-Doped CuI

Previously, we have demonstrated that the introduction of Sulfur (S) in CuI also enhances its n_h up to 6.9×10^{19} cm^{-3} (Figure 6A).[8] An additional post iodine (I_2) treatment resulted in n_h up to 5.7×10^{20} cm^{-3}. A detailed analysis indicated that S incorporation in CuI TCs results in: i) excess S at the grain boundaries forming a Cu_xS-rich phase and, ii) intragrain S helping shift the chemical potential toward I-rich conditions and thereby promoting V_{Cu} in CuI. In the case of Cs-doping we do not observe Cs segregation at the grain boundaries and the DFT defect calculations performed by Matsuzaki et al. suggest Cs helps to promote the number of V_{Cu} by forming defect complexes.[20] Furthermore, we have explained earlier that Cs-doping do not alter any structural transformations. Therefore, to leverage the role of Cs and S doping in CuI, we prepared co-doped Cs, S:CuI TCs via PLD using the same growth parameters of Cs:CuI and a target having a molar ratio of CsI:S:CuI = 0.05:0.1:1. The co-doped TC films maintain the (111) orientation with small presence of CuI monoclinic phase, as in the case of HD-Cs:CuI TC (Figure S5, Supporting Information). **Figure** 5 shows the STEM cross-section of the Cs,S:CuI film with averaged cross-sectional atomic percentages of ≈2.4 at. % and ≈1.2 at. % for Cs and S respectively. Cs and S (Figure 5) along with Cu and I (Figure S5C,D, Supporting Information) are uniformly distributed across the film.

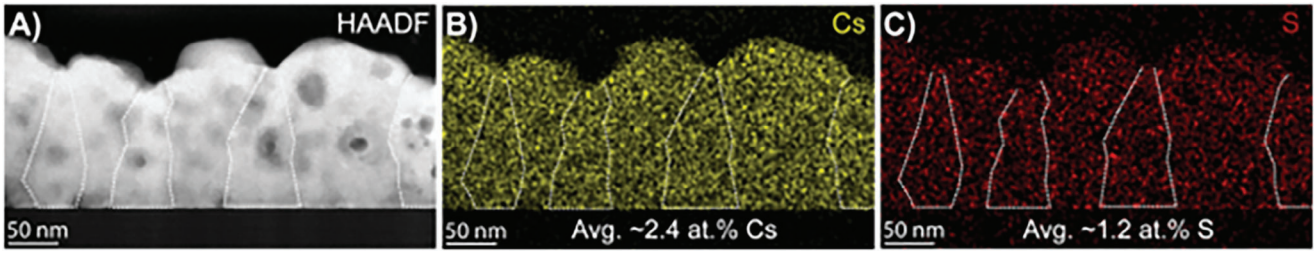

Figure 5. HAADF-STEM low magnification images depicting GBs and elemental distribution in as-deposited Cs and S co-doped CuI (Cs, S:CuI) films A) HAADF image showing columnar growth and elemental mapping of B) Cs C) S.

Figure 6A,B displays the electrical properties of intrinsic CuI, S:CuI, Cs:CuI, and Cs,S:CuI TCs. A major difference is seen in the n_h, where the co-doping results in n_h to 6.2×10^{20} cm^{-3} and a simple I_2 treatment[8] further boosts n_h to 8.2×10^{20} cm^{-3}. Consequently, μ_h drops to 3.2 cm^2 V^{-1} s^{-1} for as-deposited Cs,S:CuI TCs and slightly increases to 4.3 cm^2 V^{-1} s^{-1} for I_2 treated Cs,S:CuI TCs (Table S5, Supporting Information). As a result, we get very high σ_h of 338.4 S cm^{-1} and 572.6 S cm^{-1} for as-deposited and I_2 treated films respectively. The average visible transmittance of 76.2% for as deposited Cs,S:CuI is similar to Cs:CuI TCs, which reduces slightly to 72.4% upon I_2 treatment (Figure 6B), although the absorptance stays below 10% for the most part of the visible spectrum in both cases. From Figure 6 and Table S5 (Supporting Information), it is evident that co-doping CuI with Cs and S is an effective way to increase the carrier density of CuI in as-deposited films, without the need of an additional I_2 treatment. The high conductivity is also stable over time as will be discussed in Section 2.5.

2.4. Study of Defect and Valence Bands

Temperature-dependent σ_h was furthermore measured for the CuI and Cs:CuI TCs (**Figure** 7A). CuI depicts a typical semiconductor behavior, that is, σ_h and n_h decrease with a decrease in temperature (Figure S6A, Supporting Information). Using the thermal activation model obeying the Arrhenius relation, a very low activation energy $E_a < 1$ meV is calculated. In the case of LD-Cs:CuI, HD-Cs:CuI, and Cs,S:CuI TCs, the σ_h is independent of temperature, suggesting a degenerate semiconductor and ionized impurity scattering as the main mobility limiting mechanism.[47] Following Yamada et al.,[9] we hypothesize that the large n_h of the Cs:CuI relates to an increased density of V_{Cu}, resulting in an increased density of acceptor levels and shifting the fermi level (E_F) inside the VB, that is, forming a degenerate semiconductor with doping.

The Pisarenko plot at room temperature shows the relation between the α and n_h following Equation 1. From the Figure 7B, the existence of a complex VB is evident, as an increase in n_h cannot be defined by a single parabolic band model (Equation 1).[48] We see an increase in the estimated Seebeck hole effective mass (m_S*) (Equation 1) from 0.9 m_e to 2.4 m_e with an increase in n_h. This is a typical behavior in material systems with multiple VBs (like $CoSb_3$, $Mg_{2(1-x)}Li_{2x}Si_{0.3}Sn_{0.7}$, $SbCrSe_3$, PbSe).[49–52] CuI has two degenerate VBs, one with higher dispersion (light holes) and the other with lower dispersion (heavy holes).[44] The theoretical values for both vary from 0.22 to 2.5 m_e respectively.[10] We propose a VB model for our low n_h (CuI) and high n_h (Cs:CuI and Cs,S:CuI) TCs as shown in Figure 7C. At low n_h, the E_F lies just outside the VB, whereas, at high n_h, the E_F moves inside the VB (degenerate semiconductor). The increase in the m_S* might then be the consequence of the acceptor states overlapping and merging with the VB for $n_h > 10^{20}$ cm^{-3}. In summary, we suggest that the low μ_h for high n_h is related to increased ionized impu-

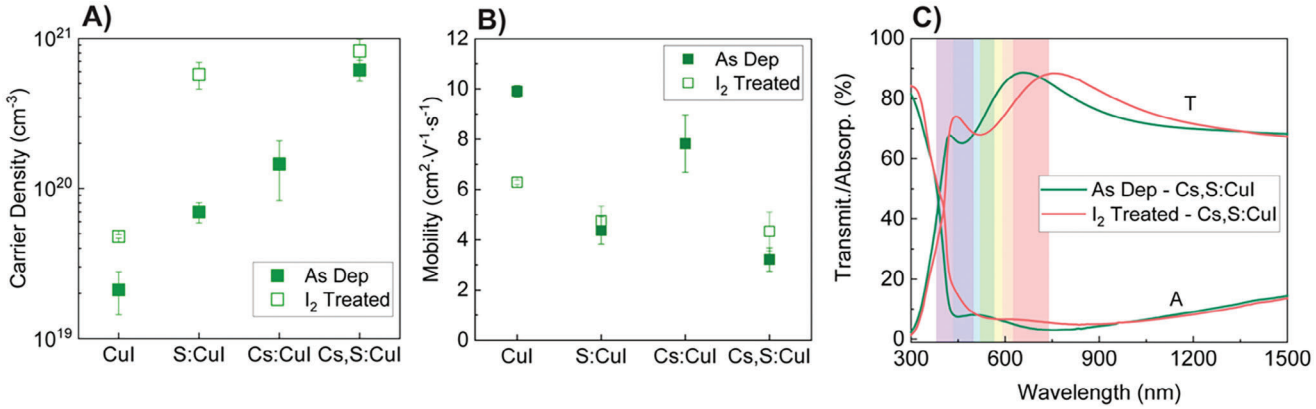

Figure 6. A) Hole carrier density and B) Hole mobility of the Cs, S:CuI TC and comparison with S:CuI, Cs:CuI and CuI, all as-deposited and iodine treated. All films have a thickness of ≈100 nm and the at. % of Cs and S in the films are summarized in Table S5 (Supporting Information). C) Transmittance (T) and Absorptance (A) of as deposited and iodine treated Cs, S:CuI TCs. Refer to Figure S5B (Supporting Information) for R data.

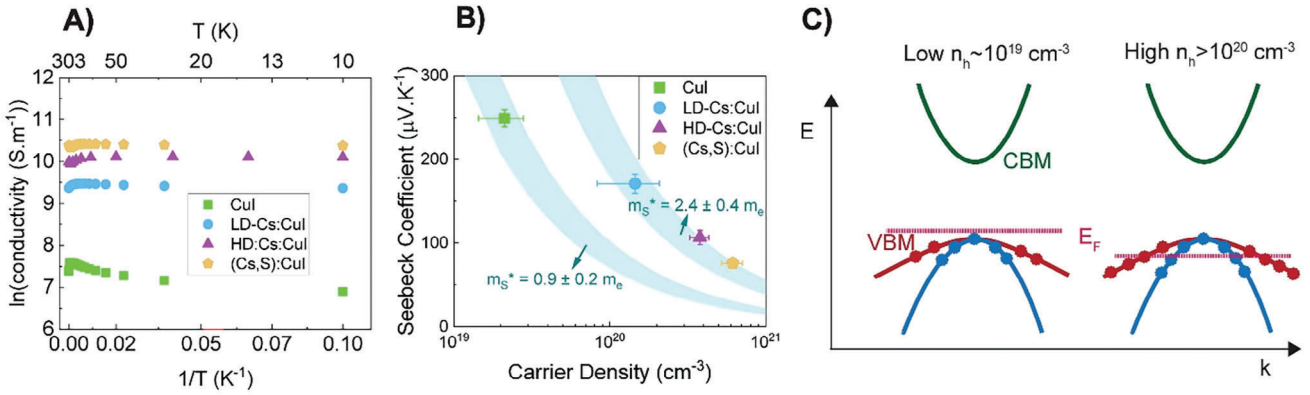

Figure 7. Defect levels and valence band model A) Temperature-dependent conductivity measurements of CuI, LD-Cs:CuI, HD-Cs:CuI, and Cs, S:CuI TCs. B) Pisarenko plot showing the relation between the Seebeck coefficient and hole carrier density. The cyan highlighted regions show range of constant Seebeck effective masses. C) Simplified band model of CuI and highly doped CuI, used only for illustration purposes.

rity scattering (as mentioned earlier) and an increase in m_S* for Cs:CuI and Cs,S:CuI films.

$$\alpha = \frac{8\pi^2 k_B{}^2 T}{3eh^2} \times m_S{}^* \times \left(\frac{\pi}{3n_h}\right)^{\frac{2}{3}} \quad (1)$$

2.5. Comparison with State-of-the-Art and Stability of CuI-Based TCs

We compared the performance of our CuI, Cs:CuI, and Cs:S:CuI with various other reported doped CuI, based on the figure of merit (FOM) defined as FOM $= \frac{\sigma_h}{\alpha_b}$. The σ_h is determined by room temperature Hall effect measurements and the α_b absorption coefficient is calculated using $\alpha_b = \frac{1}{t}\ln(\frac{1}{T})$, where t is film thickness and T is the transmittance at 550 nm. Figure 8A shows the reciprocal of the α_b plotted against σ_h. The Cs:CuI and Cs,S:CuI TCs exhibit high FOM approaching the values of ≈0.03 Ω^{-1} and are among the high reported values of CuI -based p-type TCs, just below the best performing S-doped CuI.[24,22,52,53]

The electrical instability of CuI in ambient conditions is well-known. Post-treatments with I_2[24] and H_2O_2[22] adversely affect long-term stability, primarily owing to decrease in n_h over time. On the other hand, O_2 from the ambient environment can increase n_h (and σ_h) over time, as substituted O_I acts as a shallow acceptor.[53,54] We monitored the stability of I_2-treated Cs,S:CuI, and HD-Cs:CuI films stored in an N_2 box, likely with traces of O_2. The hall effect measurements are done at ambient conditions. The HD-Cs:CuI shows a stable σ_h ≈260 S cm^{-1} for 45 days. The I_2 post-treatment in Cs, S:CuI TC shows a decrease in σ_h from ≈572 to ≈488 S cm^{-1} in a day while it stabilizes at ≈450 S cm^{-1} over a period of 44 days (Figure 8B). It stems from a decrease in n_h from 8.2×10^{20} to 6.5×10^{20} cm^{-3}. This change in σ_h does not significantly affect the FOM, as the performance of the Cs, S:CuI TC remains high (i.e., 450 S cm^{-1} with high Vis transmittance), underscoring the potential of this co-doping approach.

3. Conclusion

We have demonstrated Cs-doping and Cs, S co-doping as an effective strategy to enhance the σ_h of stable CuI-based TCs. The XRD, XAS, and STEM analysis of Cs:CuI TCs suggests that the Cs incorporation triggers no major changes in the CuI lattice,

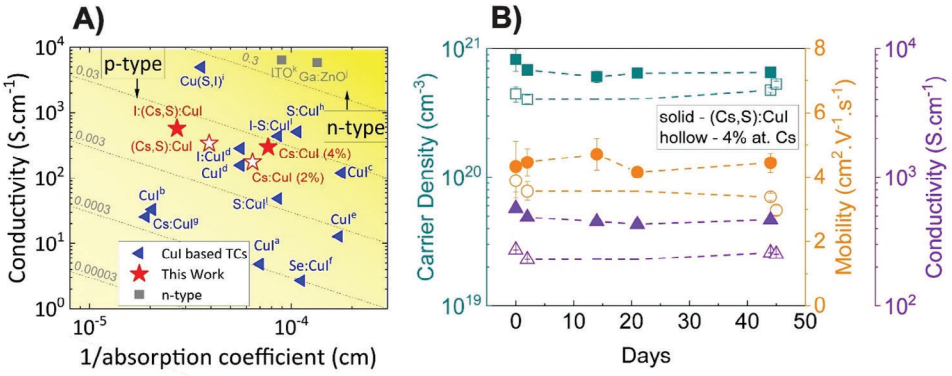

Figure 8. Performance evaluation of CuI based TCs A) Figure of merit for various doped and un-doped CuI showing the reciprocal of the absorption coefficient (at 550 nm) plotted against conductivity. The reference data is given in Table S6 (Supporting Information). Legend for deposition method: d[24]sputtering, c[14] evaporation, e[15],f,[21] l[8]PLD, a,[28] i[27] iodination, b[9]solid iodination, h[22]liquid iodination, g[20] spin coating B) Electrical stability of iodine treated Cs, S co-doped and as deposited HD-Cs:CuI TCs.

and the local structure around Cu is preserved. While the Cs are uniformly distributed for a moderate Cs doping (≈1.8 at. %) in CuI, high doping (≈4 at. %) causes non-uniform distribution of Cs along the film thickness. The electrical properties clearly show an increase in n_h as the main source of increase in σ_h with doping. The n_h increases from 2.1×10^{19} cm^{-3} for CuI to 4×10^{20} cm^{-3} for HD-Cs:CuI at the expense of reduced μ_h, with μ_h decreasing from 9.9 to ≈4 cm^2 V^{-1} s^{-1}. The n_h of co-doped Cs, S:CuI TC further increases to 6.1×10^{20} cm^{-3} ($\sigma_h = 340$ S cm^{-1}) and a subsequent post-I_2 treatment pushes it to 8.2×10^{20} cm^{-3} ($\sigma_h =$ 570 S cm^{-1}). Temperature dependent σ_h measurements confirm the degenerate semiconductor behavior for Cs:CuI and Cs,S:CuI having high $n_h > 10^{20}$ cm^{-3}, which is a clear contrast compared to the intrinsic CuI with $n_h \approx 10^{19}$ cm^{-3} presenting non-degenerate semiconductor behavior but a low $E_a < 1$ meV. Another notable effect is an increase in m_S* for high $n_h > 10^{20}$ cm^{-3}. Therefore, we suggest ionized impurity scattering and increased m_S* as the μ_h limiting mechanisms in doped CuI. In summary, our work provides an understanding of Cs incorporation in the CuI lattice and paves the way to further explore dopants that can indirectly enhance the n_h in CuI while delivering stable p-type TCs. Furthermore, room temperature growth and vacuum deposition allow future implementation in various electronic devices like solar cells and other transparent electronics.

4. Experimental Section

Target Preparation and Pulsed Laser Deposition (PLD) Deposition: The PLD targets were prepared by uniaxial pressing of CuI powders (98% Sigma–Aldrich) under a load of 7 metric tonnes. For Cs addition, targets were made by mixing CsI (99.9% Sigma–Aldrich) and CuI powders in molar ratios of ≈0.01:1:≈0.05:1 and ball milled for 3 days. For co-doping, targets were made by mixing S (98% Alfa Aesar), CsI, and CuI powders in molar ratios CsI:S:CuI = 0.05:0.1:1 ball milled and pressed as described above. Thin films were grown using a KrF (248 nm) Compex-pro laser with a frequency of 5 Hz and fluence of 2 J cm^{-2}; the deposition pressure was 0.06 mbar with Ar as background gas. The substrate was kept at room temperature. The optimization of growth parameters for CuI films is described in reference.[8] The glass and Si substrates were cleaned by 5 min sonication in acetone, ethanol, and de-ionized water sequentially before the deposition.

Note about Cs content in the PLD targets: as mentioned above, the Cs doping in CuI was introduced by adding a CsI and CuI in the targets in a molar ratio of ≈0.01:1:0.05:1 (CsI:CuI). Yet, the exact molar ratio could vary due to target fabrication uncertainties, as these were in-house prepared targets. SEM EDX on the actual PLD targets was performed to confirm the composition and the 0.01:1 target shows Cs values ranging from 1.3 at. to 1.5 at. % Cs instead of exactly 1 at. % Cs. Whereas, the 0.05:1 target shows Cs ranging from 3.5 to 4.1 at. % instead of 5 at. %. The at. % Cs percentages measured in the films via STEM/EDX indicated that the 0.01:1 and 0.05:1 target yielded ≈1.8 at. % Cs and ≈4 at. % Cs doped CuI films, respectively. Considering the uncertainties during target fabrication and error margin of the compositional measurements, the relatively small differences in Cs at. % composition in targets and films were justified.

Structural Characterization and Topography—X-Ray Diffraction (XRD): The symmetric 2θ-ω scans were done in PANalytical X'Pert3 Powder setup operating at 40 kV and 35 mA using Cu K_α radiation (1.5406 Å).

Structural Characterization and Topography—Atomic Force Microscopy (AFM): The surface morphology was measured on Bruker ICON Dimension Microscope AFM. 1 µm x 1 µm scans were done in standard air tapping mode.

Structural Characterization and Topography—Scanning Electron Microscopy (SEM): High-resolution SEM images were taken with Zeiss Merlin HR-SEM using the InLens detector mode and electron high tension (EHT) of 1.4 kV. The atomic ratios were determined using 10 kV in EDX detector mode.

Structural Characterization and Topography—X-Ray Absorption Spectroscopy (XAS): XAS measurements at the Cu K-edge (8.979 keV) were performed at beamline P65 of PETRA III at DESY in Hamburg, Germany.[55] Spectra were recorded at a temperature of ≈10 K in fluorescence mode using a 4-pixel SDD Vortex detector. Data processing and analysis were performed using the DEMETER software package,[56] with theoretical phase shifts and scattering amplitudes calculated by FEFF9.[57] The Hanning window used for FT was set to $k = 3$–13 $Å^{-1}$ with a tapering of $dk = 2$ $Å^{-1}$. Fitting was performed in radial space with $R = 1.7$–3.0 Å, $dR =$ 0.5 Å and multiple k-weights of 2,3, and 4. The coordination number was set to the zincblende value of 4 since the XANES spectra showed no signs of oxidation.[34] The same amplitude reduction factor and threshold energy were used for both films. Note that fluorescence XAS measurements at the Cs L-edges (5.0–5.8 keV) were not feasible due to the strong overlap with the simultaneously excited iodine fluorescence lines whereas measurements at the Cs K-edge (35.985 keV) were impractical for thin films due to the extremely low absorption at such high X-ray energies.

Ultraviolet Photoelectron Spectroscopy (UPS) and X-Ray Photoelectron Spectroscopy (XPS): Surface analysis by Photoemission UPS and XPS measurements was performed in a UHV chamber (ScientaOmicron) operating at a pressure of 2×10^{-9} mbar.

UPS measurements were carried out using a 21.2 eV vacuum UV source (focus). The sample was biased by 10 eV to observe the low kinetic energy cutoff. The photoelectrons were collected at an angle of 80° between the sample and analyzer, with a normal electron take off angle. The constant analyzer pass energy (CAE) was 5 eV for the valence band region and for the secondary electron cutoff (SECO).

XPS was carried out in the same spectrometer, equipped with a monochromatic Al K_α X-ray Omicron XM1000 X-ray source (hv = 1486.6 eV) operating at a power of 390 W. The high-resolution spectra were collected at a CAE of 15 eV. The XPS spectra were analyzed and quantified with CasaXPS software by integrating the peak areas using a Tougaard based background function.

Structural Characterization and Topography—Transmission Electron Microscopy (TEM) and Focused Ion Beam (FIB): For the (scanning) Transmission Electron Microscopy (S/TEM) study, A cross-sectional electron-transparent lamella was meticulously prepared using a focused ion beam (FIB) within the Scanning Electron Microscope (SEM-FIB Helios G5 DualBeam, FEI). FIB setup was equipped with an EasyLift nanomanipulator and a Gallium (Ga) ion source. To protect the region of interest during FIB processing, multiple protection layers on thin film were applied. Initially, a 0.5 µm layer of both Carbon (C) and Tungsten (W) was deposited using an electron beam (e-beam). Subsequently, an additional 3 µm layer of W was deposited by the ion beam, providing robust protection to the thin film. The ion beam milling procedure was meticulously executed in a step-by-step fashion, with decreasing beam currents (ranging from 2.4 to 0.025 nA) over an accelerating voltage range of 30–5 kV. This precise process allowed for the gradual cutting and thinning of the lamella down to a thickness of 50 nm while minimizing ion beam-induced damage. Furthermore, a low-current cleaning procedure was performed, operating at voltages ranging from 5 to 2 kV and currents from 81 to 28 pA, to ensure the removal of any potential contamination. Subsequent TEM and STEM experiments were conducted using the Cs-image corrected ThermoFisher Titan 60–300 Cubed TEM microscope at 300 keV. For scanning transmission electron microscopy (STEM), the Cs-probe corrected ThermoFisher Titan 60–300 Cubed TEM was utilized, which was equipped with a Four-Quadrant SuperX Energy Dispersive Spectrometry (EDS) Detector, and dedicated TEM holder. The acquired TEM data underwent thorough processing using specialized software packages, including Gatan Digital Micrograph and Thermo Scientific Velox suites.

Optical Characterization: Perkin Elmer Lambda 950S was used to measure the transmittance (T) and reflectance (R) of films grown on a glass substrate. The absorptance (A) was calculated using A = 100 − T − R. Deuterium and tungsten lamps were used as sources while an integrating sphere collected signals via the PMT and InGaAs detectors.

Electrical Characterization—Hall Measurements: Room temperature Hall measurements were carried out in Van der Pauw configuration and magnetic field of 1 T in ezHEMS Hall setup by NanoMagnetics. The measurements were done on 1 cm x 1 cm glass substrates with gold contacts on the corners for ohmic contact.

Temperature-dependent conductivity measurements were done in the Van der Pauw configuration using the Quantum Design Physical Properties Measurement System (PPMS). The films were deposited on 1 cm x 1 cm glass substrates with gold contacts on the corners for ohmic contact. A sweep from 9 to −9 T magnetic field was done for the resistivity measurements from 300 to 10 K. Refer to Note S1 (Supporting Information) for detailed calculations.

Electrical Characterization—Seebeck Coefficient Measurements: Seebeck measurements were taken in a home-built setup at room temperature. The thin film samples were deposited on 1 cm x 1 cm glass substrate with gold contacts on the corner and placed on Peltier elements. The current was supplied to heat one of the Peltier elements compared to the other. Voltage difference (ΔV) caused by temperature difference (ΔT) at two ends of the sample was measured. Later, the slope was extracted from the ΔT versus ΔV plot and hence the Seebeck coefficient values.

Supporting Information

Supporting Information is available from the Wiley Online Library or from the author.

Acknowledgements

The authors thank Mark Smithers for SEM EDX measurements and Dr. Melissa Goodwin and Dr. Martina Tsvetanova for FIB lamella and STEM EDX measurements of the Cs, S:CuI film. The authors also acknowledge DESY (Hamburg, Germany), a member of the Helmholtz Association HGF, for the provision of experimental facilities. Parts of this research were carried out at beamline P65 of PETRA III under proposal I-20221105. The authors are grateful to Dr. Edmund Welter and Dr. Tinku Dan for their support during the beamtime and to Dr. Konrad Ritter, Dr. Sergiu Levcenko, Hans Falk, Franziska Zahn, Sandra Montag, and Christiane Dethloff for performing the measurements. They acknowledge fruitful discussions with Dr. Mark Huijben regarding temperature-dependent conductivity measurements. The authors further acknowledge the financial support of the NWO StartUp 2019 project BRIDGE (project number. STU.019.026) and the Deutsche Forschungsgemeinschaft (DFG, German Research Foundation) under project number SCHN 1283/5-1, part of Research Unit FOR 2857.

Conflict of Interest

The authors declare no conflict of interest.

Data Availability Statement

The data that support the findings of this study are available from the corresponding author upon reasonable request.

Keywords

alkali metal doping, chalcogenide doping, charge transport, copper iodide, optoelectronics, p-type transparent conductors

Received: December 17, 2023
Revised: March 4, 2024
Published online:

[1] J. Willis, D. O. Scanlon, *J Mater Chem C Mater* **2021**, *9*, 11995.
[2] C. Körber, V. Krishnakumar, A. Klein, G. Panaccione, P. Torelli, A. Walsh, J. L. F. Da Silva, S. H. Wei, R. G. Egdell, D. J. Payne, *Phys. Rev. B* **2010**, *81*, 165207.
[3] J. Willis, I. Bravić, R. R. Schnepf, K. N. Heinselman, B. Monserrat, T. Unold, A. Zakutayev, D. O. Scanlon, A. Crovetto, *Chem. Sci.* **2022**, *13*, 5872.
[4] J. Kim, O. Kendall, J. Ren, B. J. Murdoch, C. F. McConville, J. van Embden, E. D. Gaspera, *ACS Appl. Mater. Interfaces* **2022**, *14*, 11768.
[5] P. P. Murmu, J. Kennedy, Z. Liu, T. Mori, *J. Alloys Compd.* **2022**, *921*, 166103.
[6] M. Markwitz, P. P. Murmu, S. Y. Back, T. Mori, B. J. Ruck, J. Kennedy, *Surf. Interfaces* **2023**, *41*, 103190.
[7] P. P. Murmu, V. Karthik, Z. Liu, V. Jovic, T. Mori, W. L. Yang, K. E. Smith, J. V. Kennedy, *ACS Appl. Energy Mater.* **2020**, *3*, 10037.
[8] A. S. Mirza, M. Pols, W. Soltanpoor, S. Tao, G. Brocks, M. Morales-Masis, *Matter* **2023**, *6*, 4306.
[9] N. Yamada, R. Ino, Y. Ninomiya, *Chem. Mater.* **2016**, *28*, 4971.
[10] S. Koyasu, N. Umezawa, J. D. Baniecki, A. Yamaguchi, M. Miyauchi, *Cryst. Growth Des.* **2018**, *18*, 6748.
[11] D. Chen, Y. Wang, Z. Lin, J. Huang, X. Chen, D. Pan, F. Huang, *Cryst. Growth Des.* **2010**, *10*, 2057.
[12] A. Liu, H. Zhu, M. G. Kim, J. Kim, Y. Y. Noh, *Adv. Sci.* **2021**, *8*, 2100546.
[13] R. Heasley, L. M. Davis, D. Chua, C. M. Chang, R. G. Gordon, *ACS Appl. Energy Mater.* **2018**, *1*, 6953.
[14] M. Zi, J. Li, Z. Zhang, X. Wang, J. Han, X. Yang, Z. Qiu, H. Gong, Z. Ji, B. Cao, *Phys. Status Solidi* **2015**, *212*, 1466.
[15] P. Storm, M. S. Bar, G. Benndorf, S. Selle, C. Yang, H. von Wenckstern, M. Grundmann, M. Lorenz, *APL Mater.* **2020**, *8*, 091115.
[16] S. Inagaki, M. Nakamura, Y. Okamura, M. Ogino, Y. Takahashi, L. C. Peng, X. Z. Yu, Y. Tokura, M. Kawasaki, *Appl. Phys. Lett.* **2021**, *118*, 012103.
[17] M. Nakamura, S. Inagaki, Y. Okamura, M. Ogino, Y. Takahashi, K. Adachi, D. Hashizume, Y. Tokura, M. Kawasaki, *Phys. Rev. B.* **2022**, *106*, 125307.
[18] S. Inagaki, M. Nakamura, N. Aizawa, L. C. Peng, X. Z. Yu, Y. Tokura, M. Kawasaki, *Appl. Phys. Lett.* **2020**, *116*, 192105.
[19] J. Willis, R. Claes, Q. Zhou, M. Giantomassi, G.-M. Rignanese, G. Hautier, D. O. Scanlon, *Chem. Mater.* **2023**, *35*, 8995.
[20] K. Matsuzaki, N. Tsunoda, Y. Kumagai, Y. Tang, K. Nomura, F. Oba, H. Hosono, *J. Am. Chem. Soc.* **2022**, *144*, 16572.
[21] P. Storm, M. S. Bar, S. Selle, H. von Wenckstern, M. Grundmann, M. Lorenz, *Phys. Status Solidi Rapid Res. Lett.* **2021**, *15*, 2100214.
[22] K. Ahn, G. H. Kim, S. J. Kim, J. Kim, G. S. Ryu, P. Lee, B. Ryu, J. Y. Cho, Y. H. Kim, J. Kang, H. Kim, Y. Y. Noh, M. G. Kim, *Chem. Mater.* **2022**, *34*, 10517.
[23] M. Son, G. H. Kim, O. Song, C. Park, S. Kwon, J. Kang, K. Ahn, M. G. Kim, *Adv. Sci.* **2024**, 2308188.
[24] C. Yang, M. Kneiβ, M. Lorenz, M. Grundmann, *Proc. Natl. Acad. Sci. USA* **2016**, *113*, 12929.
[25] F. Geng, L. Wang, T. Stralka, D. Splith, S. Ruan, J. Yang, L. Yang, G. Gao, L. Xu, M. Lorenz, M. Grundmann, J. Zhu, C. Yang, *Adv. Eng. Mater.* **2023**, *25*, 2201666.
[26] S. K. Maurya, Y. Liu, X. Xu, R. Woods-Robinson, C. Das, J. W. Ager, K. R. Balasubramaniam, *J Phys D Appl Phys* **2017**, *50*, 505107.
[27] F. Geng, Y. N. Wu, D. Splith, L. Wang, X. Kang, X. Chen, P. Guo, S. Liang, L. Yang, M. Lorenz, M. Grundmann, J. Zhu, C. Yang, *J. Phys. Chem. Lett.* **2023**, *14*, 6163.
[28] F. L. Schein, H. von Wenckstern, M. Grundmann, *Appl. Phys. Lett.* **2013**, *102*, 092109.
[29] M. Huangfu, Y. Shen, G. Zhu, K. Xu, M. Cao, F. Gu, L. Wang, *Appl. Surf. Sci.* **2015**, *357*, 2234.

[30] C. H. Choi, J. Y. Gorecki, Z. Fang, M. Allen, S. Li, L. Y. Lin, C. C. Cheng, C. H. Chang, *J Mater Chem C Mater* **2016**, *4*, 10309.
[31] A. Liu, H. Zhu, W. T. Park, S. J. Kang, Y. Xu, M. G. Kim, Y. Y. Noh, *Adv. Mater.* **2018**, *30*, 1802379.
[32] Grundmann, F. L. Schein, M. Lorenz, T. Böntgen, J. Lenzner, H. von Wenckstern, *Phys. Status Solidi* **2013**, *210*, 1671.
[33] Materials Project, *Data retrieved from the Materials Project for CuI (mp-673245) from database version v2023.11.1*, **2024**.
[34] E. M. Zollner, S. Selle, C. Yang, K. Ritter, S. Eckner, E. Welter, M. Grundmann, C. S. Schnohr, *Phys. Status Solidi* **2023**, *220*, 2200646.
[35] E. S. Jeong, J. Park, J. G. Park, D. S. Adipranoto, T. Kamiyama, S. W. Han, *J. Phys.: Condens. Matter* **2011**, *23*, 175402.
[36] P. Uttam, V. Kumar, K. H. Kim, A. Deep, *Mater. Des.* **2020**, *192*, 08752.
[37] W. Peng, L. Li, S. Yu, H. Zheng, P. Yang, *Appl. Surf. Sci.* **2020**, *502*, 144424.
[38] R. P. Vasquez, *Surf. Sci. Spectra 2*, 149, **1993**.
[39] T. Hellmann, M. Wussler, C. Das, R. Dachauer, I. El-Helaly, C. Mortan, T. Mayer, W. Jaegermann, *J Mater Chem C Mater* **2019**, *7*, 5324.
[40] K. Zhao, G. O. Ngongang Ndjawa, L. K. Jagadamma, A. El Labban, H. Hu, Q. Wang, R. Li, M. Abdelsamie, P. M. Beaujuge, A. Amassian, *Nano Energy* **2015**, *16*, 458.
[41] D. Obada, A. S. Mamede, N. Nuns, A. C. Grégoire, L. Gasnot, *Appl. Surf. Sci.* **2018**, *459*, 23.
[42] S. B. Fairchild, T. C. Back, P. T. Murray, M. M. Cahay, D. A. Shiffler, *J. Vac. Sci. Technol., A* **2011**, *29*, 031402.
[43] J. Zhang, S. Li, P. Yang, W. Liu, Y. Liao, *J. Mater. Sci.* **2018**, *53*, 4378.
[44] M. Graužinytė, S. Botti, M. A. L. Marques, S. Goedecker, J. A. Flores-Livas, *Phys. Chem. Chem. Phys.* **2019**, *21*, 18839.
[45] Ł. Haryński, A. Olejnik, K. Grochowska, K. Siuzdak, *Opt. Mater.* **2022**, *127*, 112205.
[46] H. Naithani, T. Dasgupta, *ACS Appl. Energy Mater.* **2020**, *3*, 2200.
[47] E. Rucavado, Defect passivation in zinc tin oxide: improving the transparency-conductivity trade-off and comparing with indium-based materials, EPFL, Laussane, **2019**.
[48] G. J. Snyder, A. Pereyra, R. Gurunathan, *Adv. Funct. Mater.* **2022**, *32*, 2112772.
[49] Y. Tang, Z. M. Gibbs, L. A. Agapito, G. Li, H. S. Kim, M. B. Nardelli, S. Curtarolo, G. J. Snyder, *Nat. Mater.* **2015**, *14*, 1223.
[50] Q. Zhang, L. Cheng, W. Liu, Y. Zheng, X. Su, H. Chi, H. Liu, Y. Yan, X. Tang, C. Uher, *Phys. Chem. Chem. Phys.* **2014**, *16*, 23576.
[51] D. Yang, W. Yao, Y. Yan, W. Qiu, L. Guo, X. Lu, C. Uher, X. Han, G. Wang, T. Yang, X. Zhou, *NPG Asia Mater* **2017**, *9*, e387.
[52] Y. Zhu, D. Wang, T. Hong, L. Hu, T. Ina, S. Zhan, B. Qin, H. Shi, L. Su, X. Gao, L.-D. Zhao, *Nat. Commun.* **2022**, *13*, 4179.
[53] P. Storm, S. Gierth, S. Selle, M. S. Bar, H. von Wenckstern, M. Grundmann, M. Lorenz, *APL Mater.* **2021**, *9*, 051101.
[54] A. Crovetto, H. Hempel, M. Rusu, L. Choubrac, D. Kojda, K. Habicht, T. Unold, *ACS Appl. Mater. Interfaces* **2020**, *12*, 48741.
[55] E. Welter, R. Chernikov, M. Herrmann, R. Nemausat, *AIP Conf. Proc.* **2019**, *2054*, 040002.
[56] B. Ravel, M. Newville, *J Synchrotron Radiat* **2005**, *12*, 537.
[57] J. J. Rehr, J. J. Kas, F. D. Vila, M. P. Prange, K. Jorissen, *Phys. Chem. Chem. Phys.* **2010**, *12*, 5503.